Journal of Computational Physics **180,** 659–685 (2002)
doi:10.1006/jcph.2002.7111

Particle Transport through Scattering Regions with Clear Layers and Inclusions

Guillaume Bal

Department of Applied Physics & Applied Mathematics, Columbia University, New York, New York 10027
E-mail: gb2030@columbia.edu

Received May 18, 2001; revised April 17, 2002

This paper introduces generalized diffusion models for the transport of particles in scattering media with nonscattering inclusions. Classical diffusion is known as a good approximation of transport only in scattering media. Based on asymptotic expansions and the coupling of transport and diffusion models, generalized diffusion equations with nonlocal interface conditions are proposed which offer a computationally cheap, yet accurate, alternative to solving the full phase-space transport equations. The paper shows which computational model should be used depending on the size and shape of the nonscattering inclusions in the simplified setting of two space dimensions. An important application is the treatment of clear layers in near-infrared (NIR) spectroscopy, an imaging technique based on the propagation of NIR photons in human tissues.

Key Words: transport equations; diffusion approximation; nonlocal boundary conditions; voids; clear layers; medical imaging.

1. INTRODUCTION

Linear transport equations are widely used to model the propagation of particles in scattering media and high-frequency waves in random media [3, 15, 19, 23, 32, 33]. Since they are posed in the phase space, transport equations are however quite expensive computationally. Consequently, they are often replaced by diffusion equations, which are posed in the position space but are only valid in highly scattering media. The approximation of transport by diffusion is well-known [12, 14, 17, 25]. It is also known that this approximation breaks down in nonscattering domains.

This paper presents generalized diffusion equations with nonlocal interface conditions at the boundary of the nonscattering inclusions. These equations, which account for the transport of particles in both the scattering and nonscattering regions, are based on an asymptotic expansion given in [8], which displays the behavior of the particle density in the vicinity of clear inclusions, and on the coupling of transport and diffusion equations

0021-9991/02 $35.00

presented in [6, 10]. One of the models presented here turns out to be equivalent to a method based on techniques borrowed from radiosity [4, 20]. A numerical analysis in the simplified setting of two space dimensions shows which computational method (classical diffusion, generalized diffusion, or transport) should be used depending on the shape of the nonscattering inclusions, the cost of the method, and the required accuracy.

The paper also displays the role of the extrapolation length in the diffusion approximation to account for the leakage of particles at the boundary of the domain.

An important application of the propagation of particles in scattering and nonscattering regions is near-infrared (NIR) spectroscopy. This imaging technique, based on the propagation of nondestructive NIR photons, is increasingly being used to monitor changes in the oxygenation of cerebral tissues, which are highly scattering media [3, 5, 20, 22, 30]. The presence of cerebrospinal fluid (CSF) within a thin clear (i.e., nonscattering) layer a few millimeters below the skull hampers the use of classical diffusion [18, 22].

The paper is organized as follows. Section 2 introduces the transport equation and its classical diffusion approximation. To simplify the numerical calculations, all equations in this paper are two dimensional and time independent. Section 3 briefly describes the numerical methods used in this paper to discretize the transport and diffusion equations and shows the role of the extrapolation length in the boundary conditions for diffusion. The derivation of the modified diffusion equations is given in Section 4. Depending on the geometry of the clear inclusions, two models are presented, in Sections 4.1 and 4.2. The variational formulation of the generalized equations, which will be used in the numerical simulations, is also given. Section 4.3 comments on the proposed models. The discretization, implementation, and relative cost of the different models are presented in Section 5. The diffusion models are numerically compared to the transport solution for several sizes of rectangular inclusions in Section 6, with some conclusions drawn in Section 6.9. A more complicated geometry of inclusions, as a toy problem to model clear layers in NIR spectroscopy, is considered in Section 7.

The simulations show the inadequacy of classical diffusion to deal with thin nonscattering inclusions and the good accuracy of the generalized diffusion models, which offer cheap alternatives to the full phase-space transport solution.

2. TRANSPORT EQUATION AND CLASSICAL DIFFUSION APPROXIMATION

The propagation of particles in scattering media can be satisfactorily modeled by a linear transport equation of Boltzmann type [14, 19]. Denoting by $\boldsymbol{x}$ and $\boldsymbol{\Omega}$ the position and direction of a particle, respectively, the phase-space flux density $u(\boldsymbol{x}, \boldsymbol{\Omega})$ of particles propagating through scattering media solves the linear transport equation

$$\begin{aligned} \boldsymbol{\Omega} \cdot \boldsymbol{\nabla} u(\boldsymbol{x}, \boldsymbol{\Omega}) + \sigma_a(\boldsymbol{x}) u(\boldsymbol{x}, \boldsymbol{\Omega}) + Q(u)(\boldsymbol{x}, \boldsymbol{\Omega}) = 0 \quad \text{in } \mathcal{D} \times V, \\ u(\boldsymbol{x}, \boldsymbol{\Omega}) = g(\boldsymbol{x}, \boldsymbol{\Omega}) \quad \text{on } \Gamma_- = \{(\boldsymbol{x}, \boldsymbol{\Omega}) \in \partial\mathcal{D} \times V \text{ s.t. } \boldsymbol{\Omega} \cdot \nu(\boldsymbol{x}) < 0\}. \end{aligned} \tag{1}$$

Here, $\mathcal{D}$ is the physical domain and V the velocity space. The vector $\nu(\boldsymbol{x})$ denotes the outward normal to $\mathcal{D}$ at $\boldsymbol{x} \in \partial\mathcal{D}$. In most physical applications, including the propagation of photons in human tissues introduced in the introduction, $\mathcal{D}$ is a three-dimensional space (although we refer to [9] for an application of genuinely two-dimensional transport equations). For computational reasons, we shall restrict ourselves in this paper to the two-dimensional setting, $\mathcal{D} \subset \mathbb{R}^2$. The velocity space is chosen to be the unit circle $V = S^1$ and we define

$\boldsymbol{\Omega} = (\cos\theta, \sin\theta)$ with $\theta \in (0, 2\pi)$. We also identify $u(\boldsymbol{x}, \boldsymbol{\Omega}) = u(\boldsymbol{x}, \theta)$. The scattering operator $Q(u)$ is defined by

$$Q(u)(\boldsymbol{x}, \boldsymbol{\Omega}) = \sigma_s(\boldsymbol{x}) \left(u(\boldsymbol{x}, \boldsymbol{\Omega}) - \frac{1}{2\pi} \int_0^{2\pi} u(\boldsymbol{x}, \theta')\, d\theta' \right), \tag{2}$$

where $\sigma_s(\boldsymbol{x})$ is the scattering coefficient. The absorption coefficient σ_a and scattering operator describe the interaction of the particles with the underlying medium [19]. The term $g(x, \boldsymbol{\Omega})$ represents the source of particles entering the domain $\mathcal{D}$ through its boundary $\partial\mathcal{D}$. The results of this paper also extend to more general transport equations such as multigroup transport equations, where V is a union of concentric circles (spheres in 3D), and anisotropic transport equations, where the scattering operator $Q(u)$ takes a more general form [27].

In the regime of small absorption and large scattering, transport is known to be well approximated by diffusion. Let us introduce the small parameter ε, which measures the *mean free path*, the mean distance between two successive interactions of a particle with the underlying medium. Mathematically, the *diffusive regime* is valid when the absorption coefficient in (1) is replaced by $\varepsilon\sigma_a(\boldsymbol{x})$ and the scattering coefficient in (2) by $\varepsilon^{-1}\sigma_x(\boldsymbol{x})$ and when the parameter ε is sufficiently small.

The derivation of the diffusion approximation to particle transport has been widely addressed in the literature [12, 14, 17, 25, 27]. The method of asymptotic expansions, which consists of analyzing the limit of the transport solution $u(\boldsymbol{x}, \boldsymbol{\Omega})$ as $\varepsilon \to 0$, is particularly well suited to the analysis of boundary effects and embedded voids, which will be taken on in subsequent sections. Following [17], for instance, the asymptotic expansion method tells us that, except in the vicinity of the boundary $\partial\mathcal{D}$, we have

$$u(\boldsymbol{x}, \boldsymbol{\Omega}) = u_0(\boldsymbol{x}) - \frac{\varepsilon}{\sigma_s(\boldsymbol{x})} \boldsymbol{\Omega} \cdot \boldsymbol{\nabla} u_0(\boldsymbol{x}) + O(\varepsilon^2), \tag{3}$$

where u_0 solves the diffusion equation

$$\begin{aligned} -\nabla D(\boldsymbol{x}) \boldsymbol{\nabla} u_0(\boldsymbol{x}) + \sigma_a(\boldsymbol{x}) u_0(\boldsymbol{x}) &= 0 \quad \text{in } \mathcal{D}, \\ u_0(\boldsymbol{x}) + 2\varepsilon L_2 D(\boldsymbol{x}) \nu(\boldsymbol{x}) \cdot \boldsymbol{\nabla} u_0(\boldsymbol{x}) &= \Lambda(g(\boldsymbol{x}, \boldsymbol{\Omega})) \quad \text{on } \partial\mathcal{D}. \end{aligned} \tag{4}$$

Here, the diffusion coefficient $D(\boldsymbol{x})$ is given by

$$D(\boldsymbol{x}) = \frac{1}{2\sigma_s(\boldsymbol{x})}, \tag{5}$$

where the unusual factor 2 comes from the choice of the velocity domain $V = S^1$. The operator Λ is a linear form that maps any incoming distribution g to a real number. Explicit expressions can be found in [15, 17], for instance. In the sequel, it will be sufficient to remark that $\Lambda(g) = g$ when g is independent of the direction $\boldsymbol{\Omega}$. The constant $L_2 = \Lambda(-\boldsymbol{\Omega} \cdot \nu(\boldsymbol{x}))$ is the *extrapolation length*. An approximate value is $L_2 = 0.8164$ [9] (instead of $L_3 = 0.7104$ when $V = S^2$). The solution of the diffusion equation (4) with Robin boundary conditions provides therefore an approximation of order $O(\varepsilon^2)$ to the direction-averaged transport density away from the boundaries (in the vicinity of the boundary, boundary layer terms need be added [9, 17]).

Remark. This paper considers only steady equations. However, it is straightforward to incorporate time dependence. At the transport level, the term $c^{-1}\partial_t u(\boldsymbol{x}, \boldsymbol{\Omega})$ should be added on the left hand side of (1), where c is the speed of the particles. In the diffusive regime, this translates into adding the terms $c^{-1}\partial_t u_0(\boldsymbol{x})$ on the left hand side of (4), respectively (see [17] for the details). The generalized diffusion equations derived in subsequent sections can be modified similarly.

3. NUMERICAL IMPLEMENTATION OF TRANSPORT AND CLASSICAL DIFFUSION

There exists a rich literature on the numerical comparison of transport and classical diffusion models [13, 24, 27]. There are also numerous methods to discretize the transport equation (1) [17, 19, 29] and the diffusion equation (4) [16]. This section presents the classical algorithms that will be used in this paper to solve the transport and generalized diffusion equations and displays the role of the extrapolation length L_2 in (4).

We assume in all numerical simulations that $\mathcal{D} = (0, 1)^2$ is the two-dimensional square. We also define $\boldsymbol{x} = (x, y)$. We use the standard diamond discretization (DD) method for the transport equation. In this method, the direction variable is discretized by using N_a uniformly distributed points on the unit circle, and the spatial variables by using a mesh of $N_x \times N_y$ uniform cells of area $h_x \times h_y$ on the square $\mathcal{D}$. We refer to [29] for the details. The advantage of this method is its second-order accuracy and simplicity of implementation. The diffusion equation is also solved by using a second-order accurate discretization based on the Q_1 finite element method. The discrete diffusion solution and the test functions are continuous and linear both in x and y on every cell of the discretization (see, for instance, [16]).

The number of unknowns in the transport equation, on the order of $N_a \times N_x \times N_y$, is too large to allow us to construct a matrix and invert it. We have therefore used the classical source iteration method preconditioned by the Q_1 diffusion discretization [1, 2]. This acceleration has proved to be stable both for scattering and nonscattering regions numerically.

The accuracy of (3) relies on introducing an extrapolation length in (4) to account for the leakage of particles at the domain boundary [12, 17]. An approximation of the extrapolation length can be obtained by assuming that the diffusion approximation is valid up to the boundary. This is the P_1 method. It consists of assuming that the transport solution is linear in the variable of direction and of averaging the transport equation over the variable of direction (see [14, 19]). The extrapolation length obtained by doing so is $L_{\mathrm{di}} = \pi/4$ when $V = S^1$ (see [9]). This value, although asymptotically not exact, is quite close to the value $L_2 = 0.8164$ of the previous section.

In the remaining part of this section, we present a numerical simulation showing the role of the extrapolation length. The incoming distribution of particles in (1) is given by the Gaussian

$$g(\boldsymbol{x}, 0, \boldsymbol{\Omega}) = e^{-65(x-0.5)^2} \quad \text{for } (\boldsymbol{x}, \boldsymbol{\Omega}) \in (0, 1) \times V, \tag{6}$$

on the bottom side independent of $\boldsymbol{\Omega}$, and with $g(\boldsymbol{x}, \boldsymbol{\Omega}) = 0$ on the other edges of $\mathcal{D}$. We recall that $\Lambda(g) = g$ for direction-independent boundary conditions. The scattering coefficient is $\sigma_s = \varepsilon^{-1}$ and the absorption coefficient $\sigma_a = \varepsilon$, where $\varepsilon = 1/50$. The number of grid points is $N_x = N_y = 150$ and $N_a = 64$. This ensures an accuracy of the transport and diffusion solutions of less than 10^{-4} for the error terms defined in (7) below.

TABLE I

L^2-Norm of the Relative Errors $e^i_{\rm vol}$ and $e^i_{\rm no}$ for the Three Diffusion Approximations u^1 Corresponding to $L = 0.8164$, u^2 Corresponding to $L = \pi/4$, and u^3 Corresponding to $L = 0$

Error	u^1	u^2	u^3
$\lvert\mathcal{D}_1\rvert^{-1}\lVert e^i_{\rm vol}\rVert_{L^2(\mathcal{D}_1)}$	2.63×10^{-4}	1.35×10^{-3}	3.81×10^{-2}
$\lVert e^i_{\rm no}\rVert_{L^2(0,1)}$	8.14×10^{-4}	4.50×10^{-3}	1.20×10^{-1}

We consider three diffusion approximations: $u^1(\boldsymbol{x})$, solution to (4) with the asymptotic extrapolation length $L_2 = 0.8164$; $u^2(\boldsymbol{x})$, solution to (4) with the diffusion extrapolation length $L_2 = \pi/4$; and $u^3(\boldsymbol{x})$, solution to (4) with no extrapolation length $L_2 = 0$. We compare the relative error between the transport solution $u(\boldsymbol{x}, \boldsymbol{\Omega})$ and the diffusion approximations in the volume $\mathcal{D}_1 = (0.1, 0.9)^2$ and on the northern edge. We denote by $u(\boldsymbol{x}, \boldsymbol{\Omega})$ the solution of (1) and by U and $\boldsymbol{J}$ its first two moments,

$$U(\boldsymbol{x}) = \frac{1}{2\pi}\int_0^{2\pi} u(\boldsymbol{x}, \theta)\, d\theta \quad \text{and} \quad \boldsymbol{J}(\boldsymbol{x}) = \frac{1}{2\pi}\int_0^{2\pi} \boldsymbol{\Omega}\, u(\boldsymbol{x}, \theta)\, d\theta.$$

Let us define

$$e^i_{\rm vol}(\boldsymbol{x}) = \frac{U(\boldsymbol{x}) - u^i(\boldsymbol{x})}{U(\boldsymbol{x})}, \quad e^i_{\rm cur}(\boldsymbol{x}) = \frac{\boldsymbol{J}(\boldsymbol{x}) \cdot \nu(\boldsymbol{x}) - D\nu \cdot \boldsymbol{\nabla} u^i(\boldsymbol{x})}{\boldsymbol{J}(\boldsymbol{x}) \cdot \nu(\boldsymbol{x})}, \tag{7}$$

the relative errors in the volume ($\boldsymbol{x} \in \mathcal{D}$) and on the edges ($\boldsymbol{x} \in \partial\mathcal{D}$), respectively. We define $e^i_{\rm no}(\boldsymbol{x}) = e^i_{\rm cur}(\boldsymbol{x})$ if $\boldsymbol{x}$ belongs to the northern edge of $\mathcal{D}$ and $e^i_{\rm ea}(\boldsymbol{x}) = e^i_{\rm cur}(\boldsymbol{x})$ if $\boldsymbol{x}$ belongs to the eastern edge.

The L^2-norm, which is defined for a function $f(\boldsymbol{x})$ on a domain X by $\lVert f\rVert_{L^2(X)} = (\int_X |f(\boldsymbol{x})|^2\, d\boldsymbol{x})^{1/2}$, of relative errors is shown in Table I (the volume of a domain X is denoted $|X|$). The L^2-norm of the error $e^i_{\rm vol}$ is compatible with theory, $e^3_{\rm vol}$ being of order

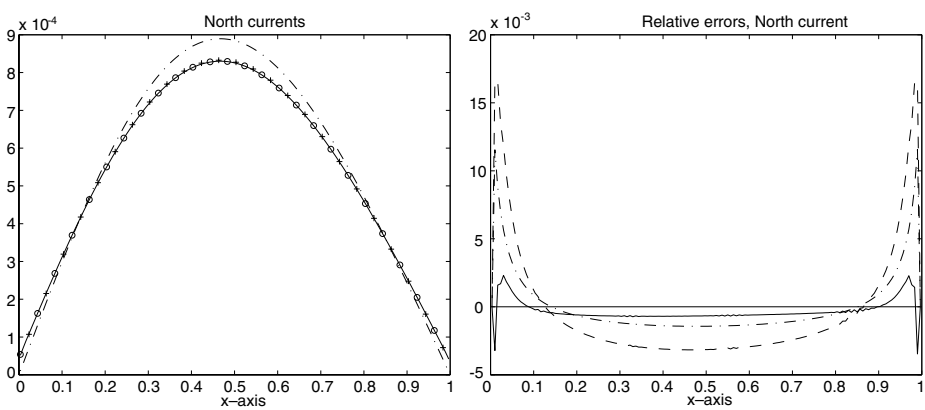

FIG. 1. Currents on the upper edge of $\mathcal{D}$ of the solutions to (1) and (4). (Left) Transport current $\boldsymbol{J}(\boldsymbol{x}) \cdot \nu(\boldsymbol{x})$ (solid line) and diffusion currents $D\nu \cdot \boldsymbol{\nabla} u^i(\boldsymbol{x})$ for u^1 (dotted line with circles), for u^2 (dotted line with crosses), and for u^3 (dot–dashed line). (Right) Relative errors $e^i_{\rm no}(\boldsymbol{x})$ in (7) on the upper edge of $\mathcal{D}$. Error $e^1_{\rm no}$, solid line; error $e^2_{\rm no}$, dashed line; $\varepsilon \times$ error $0.02e^3_{\rm no}$, dot–dashed line.

ε and $e^1_{\rm vol}$ of order ε^2. The intermediate solution u^2 captures most of the error made by the least accurate u^3 but is still not as accurate as u^1.

Important in practice, in particular for solving inverse problems, is the current distribution at the domain boundary. We have represented in Fig. 1 the currents obtained on the upper edge of the domain. The figure on the left side shows that all diffusion approximations except u^3 provide visually correct estimations of the current distribution. The figure on the right side shows that u^3 is one order of magnitude less accurate than the other approximations ($\varepsilon e^3_{\rm no} = e^3_{\rm no}/50$ is shown in Fig. 1), and that u^1 still provides a much more accurate description of the currents in spite of the unresolved boundary layers.

4. MODELS FOR TRANSPORT THROUGH SCATTERING AND NONSCATTERING REGIONS

The diffusion approximation discussed in the previous section holds only in highly scattering media. We will see in the next section that the classical diffusion approximation gives completely erroneous results when thin embedded voids are present. A way to overcome this problem is to solve the phase-space transport equation in the whole domain. However, even though modern computers now allow us to solve three-dimensional transport equations routinely [35], the solutions are still fairly expensive, especially when the ultimate goal, namely inverting the optical properties of tissues from boundary measurements, requires the solution of many forward problems. Let us mention that hybrid transport-diffusion methods (see, for instance, [10] for a deterministic algorithm and [21] for a Monte Carlo method with diffusion-based acceleration), local refinements of the spatial discretization [7, 11], or mean-free-path-independent numerical algorithms [26, 28] can also be used to reduce the cost of transport.

The main result of this paper is that generalized diffusion equations can account for the propagation of particles in both scattering and nonscattering domains provided the latter satisfy some geometrical constraints. The generalized models are more expensive than classical diffusion (but classical diffusion is useless), but much less costly than full transport (and still relatively accurate).

4.1. Large Embedded Inclusions

We consider two types of nondiffusive regions in this paper. The first one models an embedded object of size comparable to $\mathcal{D}$, that is to say, large compared to the mean free path ε. Let $\mathcal{D}^C$ be such a subdomain of $\mathcal{D}$. We denote by $\mathcal{D}^E = \mathcal{D}\backslash\overline{\mathcal{D}^C}$ its complementary and assume that the embedded object $\mathcal{D}^C$ does not touch the boundary of $\mathcal{D}$. We assume that $\mathcal{D}^E$ is diffusive and that $\mathcal{D}^C$ is nonscattering (and allowed to be slightly absorbing). The particle transport can thus be modeled by the equation

$$\begin{aligned}
&\boldsymbol{\Omega}\cdot\boldsymbol{\nabla} u(\boldsymbol{x},\boldsymbol{\Omega}) + \frac{1}{\varepsilon} Q(u)(\boldsymbol{x},\boldsymbol{\Omega}) + \varepsilon\sigma_a(\boldsymbol{x}) u(\boldsymbol{x},\boldsymbol{\Omega}) = 0 && \text{in } \mathcal{D}^E \times V,\\
&u(\boldsymbol{x},\boldsymbol{\Omega}) = g(\boldsymbol{x},\boldsymbol{\Omega}) && \text{on } \Gamma_-,\\
&\boldsymbol{\Omega}\cdot\boldsymbol{\nabla} u^c(\boldsymbol{x},\boldsymbol{\Omega}) + \varepsilon\sigma_a u^c(\boldsymbol{x},\boldsymbol{\Omega}) = 0 && \text{in } \mathcal{D}^C \times V,\\
&u(\boldsymbol{x},\boldsymbol{\Omega}) = u^c(\boldsymbol{x},\boldsymbol{\Omega}) && \text{on } \partial\mathcal{D}^C \times V.
\end{aligned} \tag{8}$$

The last equation corresponds to the continuity of the particle density across the interface

$\partial\mathcal{D}^C$. The generalization of the asymptotic expansions used in Section 2 to the coupled problem (8) has been analyzed in [8]. In that paper, it is shown that the solution u to the coupled equation (8) can be decomposed as $u = u_0 + O(\varepsilon)$, where u_0 solves the diffusion equation

$$\begin{aligned} &-\nabla D(\boldsymbol{x})\nabla u_0(\boldsymbol{x}) + \sigma_a(\boldsymbol{x})u_0(\boldsymbol{x}) = 0 \quad \text{in } \mathcal{D}^E, \\ &u_0(\boldsymbol{x}) = \Lambda(g(\boldsymbol{x}, \boldsymbol{\Omega})) \quad \text{on } \partial\mathcal{D}, \\ &u_0(\boldsymbol{x}) = \text{Constant} \quad \text{on } \partial\mathcal{D}^C, \\ &\int_{\partial\mathcal{D}^C} D(\boldsymbol{x})\nu^E \cdot \nabla u_0(\boldsymbol{x})\, d\Sigma(\boldsymbol{x}) + u_{0|\partial\mathcal{D}^C} \int_{\mathcal{D}^C} \sigma_a(\boldsymbol{y})\, d\boldsymbol{y} = 0, \end{aligned} \tag{9}$$

where $d\Sigma$ is the usual surface measure on $\partial\mathcal{D}^C$. Notice that the local diffusion equilibrium $u(\boldsymbol{x}, \boldsymbol{\Omega}) = u(\boldsymbol{x})$ of Section 2 is replaced by the *nonlocal* equilibrium $u_0 = \text{Cst}$ on $\partial\mathcal{D}^C$ (and actually on $\boldsymbol{\Omega}^C$ as well). The last equality in (9) ensures particle conservation across $\partial\mathcal{D}^C$.

Remark. We can check that Eq. (9) can also be obtained from the diffusion equation (4) by formally sending the diffusion coefficient $D(\boldsymbol{x})$ to infinity on $\mathcal{D}^C$ (see also [8]). This is consistent with the definition of the diffusion coefficient (5), where σ_s in the highly scattering domain is replaced by $\varepsilon\sigma_s$ in the non-highly-scattering domain. Therefore, even though the derivation of (4) in Section 2 is not correct physically, it will still provide the correct result (9) asymptotically.

4.2. Thin Clear Layers and Transport-Diffusion Coupling

For thin extended clear layers, the second type of inclusions considered is this paper, the situation is more complicated and classical diffusion equations will provide very poor approximations to transport. By a thin extended clear layer, we mean an inclusion that has an $O(1)$ extension in one dimension and a $O(L_\varepsilon)$ thickness in the other direction (see Fig. 2), where L_ε is a dimensionless small parameter different from ε (see below). We know from the preceding section that the solution becomes asymptotically constant inside the inclusion as $\varepsilon \to 0$ when the inclusion is a domain independent of ε. The only way to obtain a richer asymptotic limit is therefore to mathematically correlate the geometry of the inclusion with the mean free path ε. The results of [8], where the asymptotic expansion method is extended to this new geometry, show that a generalized diffusion equation with nonlocal boundary conditions can be obtained when the thickness of the clear layer is such that $L_\varepsilon^2 |\ln L_\varepsilon| = \varepsilon$,

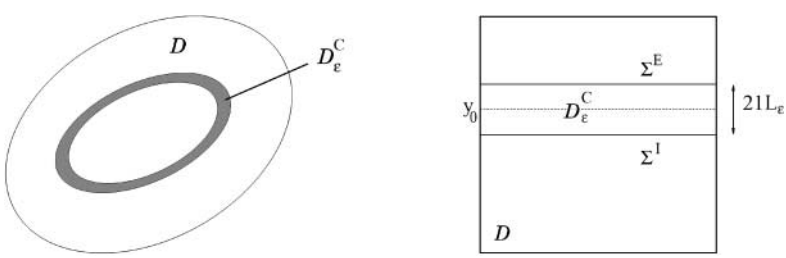

FIG. 2. (Left) Geometry of the clear layer. The external and internal regions $\mathcal{D}\backslash\mathcal{D}_\varepsilon^C$ are diffusive, whereas the clear layer $\mathcal{D}_\varepsilon^C$ is not. (Right) Geometry of a straight clear layer.

that is to say, up to logarithmic corrections, when the thickness of the layer L_ε scales as $\sqrt{\varepsilon}$, the square root of the mean free path.

We shall not reproduce the analysis of [8] here. Its salient feature for our purpose here is that the difference between the transport and generalized diffusion solutions is of order $O(\varepsilon)$ everywhere. This means that to accurately describe the transport equation no boundary layer is necessary in the vicinity of the interface separating the scattering and nonscattering regions. This remark is important because it allows us to use the results on the coupling of transport and diffusion equations in [6, 10] to derive a more accurate diffusion equation than the generalized equation in [8] obtained by asymptotic expansions.

The main idea is that when no boundary layer term is necessary, it is possible to use a diffusion approximation in the diffusive region, a transport model in the nondiffusive one, and a coupling between the two equations at their common interface based on current conservation. The transport-diffusion coupling analyzed in [6, 10] proceeds as follows. We split the physical domain $\mathcal{D}$ into two subdomains, $\mathcal{D}_{\rm di}$ and $\mathcal{D}_{\rm tr}$, where $\mathcal{D}_{\rm di}$ is diffusive and $\mathcal{D}_{\rm tr}$ is not. Let γ be their common interface and $\gamma_- = \{(\boldsymbol{x}, \boldsymbol{\Omega}) \in \gamma \times V,\ \boldsymbol{\Omega} \cdot \nu_\gamma(\boldsymbol{x}) < 0\}$, where $\nu_\gamma(\boldsymbol{x})$ is the outward unit normal to $\mathcal{D}_{\rm tr}$ at $\boldsymbol{x} \in \gamma$. We denote by $U(\boldsymbol{x})$ the diffusion solution on $\mathcal{D}_{\rm di}$ and $u(\boldsymbol{x}, \boldsymbol{\Omega})$ the transport solution on $\mathcal{D}_{\rm tr}$. The volume equations are then

$$\boldsymbol{\Omega} \cdot \boldsymbol{\nabla} u(\boldsymbol{x}, \boldsymbol{\Omega}) + \sigma_a(\boldsymbol{x}) u(\boldsymbol{x}, \boldsymbol{\Omega}) + Q(u)(\boldsymbol{x}, \boldsymbol{\Omega}) = 0 \quad \text{in } \mathcal{D}_{\rm tr} \times V, \tag{10}$$

$$-\nabla D(\boldsymbol{x}) \boldsymbol{\nabla} U(\boldsymbol{x}) + \sigma_a(\boldsymbol{x}) U(\boldsymbol{x}) = 0 \quad \text{in } \mathcal{D}_{\rm di}. \tag{11}$$

They are augmented with the classical (transport or diffusion) boundary conditions on $\partial\mathcal{D}$. It remains to define the interface conditions. Notice that in (10), scattering is still permissible in the transport region. However, in the application of clear layers, we will have a much simpler transport equation since $\sigma_a(\boldsymbol{x}) = \sigma_s(\boldsymbol{x}) = 0$ on $\mathcal{D}_{\rm tr}$. We now consider two types of interface conditions.

4.2.1. *Model 1*

Following the linear expansion in $\boldsymbol{\Omega}$ of the transport solution in the diffusion approximation, we impose that

$$u(\boldsymbol{x}, \boldsymbol{\Omega}) = U(\boldsymbol{x}) - \frac{1}{\sigma_s(\boldsymbol{x})} \boldsymbol{\Omega} \cdot \boldsymbol{\nabla} U(\boldsymbol{x}) \quad \text{on } \gamma_-. \tag{12}$$

This model retains the leading term and the first-order perturbation in the expansion (3). The second interface condition is obtained by enforcing current conservation,

$$\frac{1}{2\pi} \int_0^{2\pi} \boldsymbol{\Omega} \cdot \nu(\boldsymbol{x})\, u(\boldsymbol{x}, \boldsymbol{\Omega})\, d\theta = D(\boldsymbol{x}) \nu \cdot \boldsymbol{\nabla} U(\boldsymbol{x}) \quad \text{on } \gamma. \tag{13}$$

It is shown in [6, 10] that the above four equations with suitable conditions on $\partial\mathcal{D}$ form a well-posed problem. Notice that (12) can be seen as a Dirichlet boundary condition for the transport equation and (13) as a Neumann boundary condition for diffusion.

Let us apply this model to the problems in Sections 4.1 and 4.2 to the case of voids; that is to say, the nondiffusive region is completely nonscattering and nonabsorbing ($\sigma_s = \sigma_a = 0$), although the generalization to absorbing media is straightforward. Let us assume for concreteness that the nondiffusive region $\mathcal{D}_{\rm tr} = \mathcal{D}^C$ is the straight layer given on the right of Fig. 2 (hence $\nu = (0, 1)$ in the rest of this section, so that $\boldsymbol{\Omega} \cdot \nu = \sin\theta$), and the

diffusive region $\mathcal{D}_{\rm di}$ is $\mathcal{D}\backslash\mathcal{D}^C$. We then recast (13) using (12) for $x \in \Sigma^E \subset \gamma$ as

$$\begin{aligned}\frac{1}{2\pi}\int_0^{2\pi} \sin\theta\, u(\boldsymbol{x},\theta)\,d\theta &= \frac{1}{2\pi}\int_0^{\pi} \sin\theta\, u(\boldsymbol{x},\theta)\,d\theta + \frac{1}{2\pi}\int_{\pi}^{2\pi} \sin\theta\, u(\boldsymbol{x},\theta)\,d\theta\\ &= \frac{1}{2\pi}\int_0^{\pi} \sin\theta\, u(\boldsymbol{x},\theta)\,d\theta + \frac{1}{2\pi}\int_{\pi}^{2\pi} \sin\theta\, U(\boldsymbol{x})\,d\theta\\ &\quad - \frac{1}{2\pi\sigma_s(\boldsymbol{x})}\int_{\pi}^{2\pi} \sin\theta\, \boldsymbol{\Omega}\cdot\nabla U(\boldsymbol{x})\,d\theta\\ &= \frac{1}{2\pi}\int_0^{\pi} \sin\theta \left(\mathcal{R}^c u_{|\Sigma^I}\right)(\boldsymbol{x},\theta)\,d\theta - \frac{1}{\pi}U(\boldsymbol{x}) + \frac{1}{4\sigma_s(\boldsymbol{x})}\frac{\partial U}{\partial x_2}(\boldsymbol{x})\\ &= D(\boldsymbol{x})\frac{\partial U}{\partial x_2}(\boldsymbol{x}).\end{aligned}$$

The operator $\mathcal{R}^c$ is the transport solution operator, which maps what enters the clear layer to what exits the clear layer. In general, the definition of this operator involves solving a complicated transport equation in $\mathcal{D}_{\rm tr} \times V$. When σ_a and σ_s vanish inside the clear layer, however, this operator is easily calculated. Since particles travel along straight lines in the clear layer, we obtain for $x \in \Sigma^E$ that

$$(\mathcal{R}^c u)(\boldsymbol{x},\theta) = u(\boldsymbol{x} - 2lL_\varepsilon \cot\theta\boldsymbol{\Omega},\theta), \tag{14}$$

where the point $\boldsymbol{x} - 2lL_\varepsilon \cot\theta\boldsymbol{\Omega}$ belongs to Σ^I. Since $D = (2\sigma_s)^{-1}$, according to (5), we obtain that

$$D\frac{\partial U}{\partial x_2} + \frac{2}{\pi}U(\boldsymbol{x}) = \frac{1}{\pi}\int_0^{\pi} \sin\theta \left(\mathcal{R}^c u_{|\gamma_-}\right)(\boldsymbol{x},\theta)\,d\theta. \tag{15}$$

Let us now replace $u_{|\gamma_-}$ by its expression in (12). This yields for U the nonlocal boundary condition

$$D\frac{\partial U}{\partial x_2} + \frac{2}{\pi}U(\boldsymbol{x}) = \frac{1}{\pi}(G_0[U](\boldsymbol{x}) - G_1[U](\boldsymbol{x})), \tag{16}$$

where

$$\begin{aligned}G_0[U](\boldsymbol{x}) &= \int_0^{\pi} \sin\theta (\mathcal{R}^c U)(\boldsymbol{x},\theta)\,d\theta,\\ G_1[U](\boldsymbol{x}) &= \int_0^{\pi} \sin\theta \left(\mathcal{R}^c \frac{\boldsymbol{\Omega}\cdot\boldsymbol{\nabla} U}{\sigma_s}\right)(x,\theta)\,d\theta.\end{aligned} \tag{17}$$

This defines Model 1. The definition of the above terms can then be generalized to other orientations of the boundary normal ν.

4.2.2. *Model 2*

Another model consists of retaining only the leading term in the expansion (3) and using the same generalized boundary condition (15). The nonlocal boundary condition (16) for U is then replaced by

$$D\frac{\partial U}{\partial x_2} + \frac{2}{\pi}U(\boldsymbol{x}) = \frac{1}{\pi}\int_0^{\pi} \sin\theta (\mathcal{R}^c U)(\boldsymbol{x},\theta)\,d\theta. \tag{18}$$

Following the same calculations as in the previous section, we see that the current conservation (13) is now replaced by

$$\frac{1}{\pi}\int_0^{2\pi} \Omega\cdot\nu(x)\,u(x,\Omega)\,d\theta = D(x)\nu\cdot\nabla U(x) \quad \text{on } \gamma. \tag{19}$$

Therefore, current conservation is no longer imposed in this model (a factor 2 is missing). Notice however that both currents tend to 0 as the mean free path tends to 0. Therefore, only an equation of the order of the mean free path ε is not correctly satisfied.

In the three-dimensional setting, the above equality needs to be replaced by

$$D\nu\cdot\nabla U + \frac{1}{2}U(x) = \frac{1}{4\pi}\int_{V^+} \Omega\cdot\nu(\mathcal{R}^c U)(x,\Omega)\,d\Omega, \tag{20}$$

where V^+ is the set of outgoing directions at x and $d\Omega$ the usual solid-angle measure. This relation is equivalent to the hybrid radiosity-diffusion theory proposed in [4, 20]. It has also been analyzed as a transport-diffusion coupling in [34].

4.2.3. *Variational Formulation*

Let us define $m = 1$ for Model 1 and $m = 0$ for Model 2. The diffusion equation with nonlocal boundary conditions (11)–(16) on γ and local boundary conditions on $\partial\mathcal{D}$ is now a closed equation for U on $\mathcal{D}_{\rm di}$:

$$\begin{aligned} &-\nabla D(x)\nabla U(x) + \sigma_a(x)U(x) = 0 && \text{in } \mathcal{D}\backslash\mathcal{D}^C,\\ &U(x) + 2LD(x)\nu\cdot\nabla U(x) = \Lambda(g(x)) && \text{on } \partial\mathcal{D},\\ &D\nu\cdot\nabla U + \frac{2}{\pi}U = \frac{1}{\pi}(G_0[U] - mG_1[U]) && \text{on } \partial\mathcal{D}^C. \end{aligned} \tag{21}$$

Its variational formulation is as follows: Find $U \in H^1(\mathcal{D}_{\rm di})$ such that for every test function $\phi \in H^1(\mathcal{D}_{\rm di})$, we have

$$\begin{aligned} &\int_{\mathcal{D}_{\rm di}} (D\nabla U\cdot\nabla\phi + \sigma_a U\phi)\,dx + \int_\gamma \frac{\phi}{\pi}(2U - G_0[U] + mG_1[U])\,d\Sigma(x)\\ &\quad + \int_{\partial\mathcal{D}} \frac{1}{2L}U\phi\,d\Sigma(x) = \int_{\partial\mathcal{D}} \frac{1}{2L}\Lambda(g)\phi\,d\Sigma(x). \end{aligned} \tag{22}$$

Here, $d\Sigma$ denotes the usual surface measure.

The variational formulation (22) lends itself very naturally to the discretization by any Galerkin method, such as the Q_1 finite element method chosen in this paper.

4.3. Interpretation of the Models

We have obtained two different types of generalized diffusion equations that account for nonscattering and nonabsorbing inclusions. When the inclusion is large, the solution tends to be uniformly constant inside the inclusion, provided the mean free path is sufficiently small (see (9)). Classical diffusion can then be used. When the inclusion is thin in one direction (such as for clear layers), it plays the role of a waveguide that is not captured

by classical diffusion. Generalized diffusion equations with nonlocal boundary conditions must then be used. An important property obtained from asymptotic expansions is that no boundary layer is necessary in the vicinity of the inclusion to approximate the transport solution (at least in the leading order; there are boundary layers of size $O(\varepsilon)$). This allowed us to derive a method based on solving the diffusion equation in the diffusive domain and the transport equation in the inclusions, and on coupling the two solutions at their common interface.

Depending on the choice of the coupling (first-order or second-order accurate), two models have been presented. Model 1 is a priori more accurate than Model 2 since more terms are retained in the asymptotic expansion (3). However, both models are asymptotically of order $O(\varepsilon)$, as boundary layer terms of order $O(\varepsilon)$ are not accounted for. Moreover, Model 1 involves the gradient $\boldsymbol{\Omega} \cdot \boldsymbol{\nabla} U$ over the whole surface γ; hence it is more expensive to solve and implement. We will see that Model 1 is actually significantly more accurate than Model 2 in most situations.

The nonlocal boundary conditions of Models 1 and 2 can be generalized to more complicated geometries in a straightforward manner. For complicated geometries, however, the calculation of the solution operator $\mathcal{R}^c$ becomes more involved and requires knowing at each point $\boldsymbol{x}$ of the boundary γ all the other visible points $\boldsymbol{y} \in \gamma$ such that the segment $(\boldsymbol{x}, \boldsymbol{y})$ does not intersect γ. The feasibility and efficiency of ray tracing will then become a crucial ingredient of the method, an important aspect that we consider in this paper.

5. IMPLEMENTATION AND RELATIVE COST OF TRANSPORT AND CLASSICAL AND GENERALIZED DIFFUSION

This section and the following two sections are devoted to the numerical implementation of the diffusion approximations presented in the preceding sections and their comparison with transport. The geometry is that of a scattering domain $\mathcal{D} = (0, 1)^2$ with embedded voids of various shapes.

We denote by $u(\boldsymbol{x}, \boldsymbol{\Omega})$ the solution of the diamond discretization of the transport equation (8) and by $U(\boldsymbol{x})$ its average over the discrete ordinates. We consider the discretization of four diffusion approximations. The solution of Model 1 is denoted $u^1(\boldsymbol{x})$ and that of Model 2 $u^2(\boldsymbol{x})$. The solution of the classical diffusion model, which is also the solution to (9) since the diffusion coefficient is infinite in voids, is denoted $u^3(\boldsymbol{x})$. We also consider a fourth diffusion solution $u^4(\boldsymbol{x})$, where the voids have been replaced by the same scattering medium as the rest of the domain (u^4 is therefore the solution of the diffusion equation in a homogeneous domain). In the subsequent sections, we refer to $U(\boldsymbol{x})$ as the transport solution, to which the diffusion models $u^i(\boldsymbol{x})$, $i = 1, \ldots, 4$ are compared.

5.1. Numerical Implementation of the Nonlocal Interface Conditions

The numerical implementation of transport and classical diffusion has been addressed in Section 3. The implementation of the generalized diffusion equation with nonlocal interface conditions is based on the variational formulation (22). Except for the integration term over γ, all the other terms are classical in the variational formulation of elliptic problems. In the two-dimensional Q_1 approximation, the basis for the test functions ϕ is composed of piecewise bilinear functions in x and y that equal 1 at one grid point of the mesh and 0 at

the other points. Let us denote by N_i the basis function that equals 1 at the ith point of the grid and consider the case $m = 0$ to simplify. The integration along γ in (22) involves the computation of terms of the form

$$\int_\gamma \frac{N_i}{\pi}\left(2N_k - \int_0^\pi \sin\theta(\mathcal{R}^c N_k)(x,\theta)\,d\theta\right)d\Sigma \tag{23}$$

for those points i and k of the grid that are on γ. The response operator defined by (14) is easy to compute when $\mathcal{D}^C$ is a rectangle: Particles travel through the clear domain along straight lines until they leave it. By symmetry, we essentially have two cases to analyze accordingly, (1) N_i and N_k belong to opposite side or (2) they belong to adjacent side. For instance, if $N_{i|\gamma}$ is supported on the upper side and $N_{k|\gamma}$ on the lower side, (23) is recast using (14) as

$$\frac{1}{\pi}\int_\gamma N_i(x)\int_0^\pi \sin\theta(N_k(x) - N_k(x - L_x\cot\theta))\,d\theta. \tag{24}$$

After the change of variables $z = x - L_x\cot\theta$ and recalling that N_i and N_k are piecewise linear on γ, we obtain for the second term in (24) the expression

$$\frac{-h_x^2}{\pi}\int_{-1}^1 (1-|x|)\int_{j-1}^{j+1}\frac{1}{[1+(h_x(x-z)/L_x)^2]^{3/2}}\frac{1}{L_x}(1-|z-j|)\,dz\,dx, \tag{25}$$

where jh_x is the horizontal distance between the nodes N_i and N_k. Similarly, if $N_{i|\gamma}$ is supported on the lower side and $N_{k|\gamma}$ on the left side, (23) is given by

$$\frac{-h_x h_y}{\pi}\int_{Y-1}^{Y+1}(1-|y-Y|)\int_{X-1}^{X+1}(1-|x-X|)\frac{xh_x yh_y\,dx\,dy}{[(xh_x)^2+(yh_y)^2]^{3/2}}, \tag{26}$$

where Yh_y is the distance between the origin and the kth node and Xh_x is the distance between the origin and the ith node. Similar expressions are also obtained when one of the nodes is a corner of $\mathcal{D}^C$. These integrals have been computed numerically with sufficient accuracy (see next section) using a Gaussian quadrature rule. The case $m = 1$ is handled similarly. We do not report the lengthy details.

5.2. Comparison of the Costs of Transport and Diffusion

The running times indicated in this section correspond to codes written in MATLAB and running on a Pentium II 400 MHz processor with LINUX environment.

The solution of the classical diffusion equation requires two steps. The first one consists of constructing the matrix we want to invert and the source terms, and the second one of inverting the corresponding linear system. This second step has been performed by using the conjugate gradient method with incomplete LU preconditioning. Solving the generalized diffusion equations (22) requires one additional step in the construction of the matrix to invert, which accounts for the nonlocal interface conditions at the boundary of the void. The terms of the form (25) and (26) are calculated using a Gaussian quadrature rule [31].

We compare the transport and diffusion solutions in the configuration of Test 4 in Section 6.4. The domain is $\mathcal{D} = (0,1)^2$ and the inclusion $\mathcal{D}^C = (0.5, 0.6)\times(0.3, 0.7)$. The spatial discretization is the same for all solutions with $N_x = N_y = 200$.

The accuracy of the best diffusion approximation compared with the transport solution is at best of order 10^{-3}, as reported in the following section. The parameters of the diffusion and transport solutions have therefore be tuned so that the running time is minimized and the precision with respect to a corresponding very fine solution is higher than 10^{-3}.

By doing so, we found that the minimum number of points of the Gaussian quadrature rule used on every segment to calculate (25) and (26) is $N_G = 8$. The time to construct the diffusion matrix without the interface conditions and the source term is 4.5 s. The time to construct the matrix corresponding to the interface conditions is 56 s for Model 2 and 162 s for Model 1. The time to solve the diffusion problems once the matrices are constructed is about 40 s (and varies very little for the different solutions u^1, u^2, and u^3).

The total running time for the diffusion models is therefore $t_3 = 45$ s for the classical diffusion solution u^3, $t_2 = 106$ s for the solution u^2 of Model 2, and $t_1 = 212$ s for the solution u^1 of Model 1. In comparison, the total running time of the transport solution is $t_u = 3.5 \times 10^3$ s. It was obtained after 22 iterations of the source iteration method preconditioned by the Q_1 diffusion solver. The necessary number of directions is $N_a = 16$. The time spent in the diffusion acceleration is negligible compared to the free transport solutions obtained at each iteration of the source iteration method.

We therefore find that the classical diffusion solution u^3 is $\rho_3 = 78$ times faster than the transport solution, and that the generalized diffusion solutions u^1 and u^2 are $\rho_1 = 17$ and $\rho_2 = 33$ times faster than the transport solution, respectively.

Remark. Although the generalized diffusion solutions above remain more than 1 order of magnitude less expensive than the transport solution, they are still significantly more expensive than the classical diffusion equations. We believe that the latter ratio can be improved. The complexity of calculating the matrix corresponding to the interface conditions is at most proportional to $N_G^2 n_x n_y$, where the layer is composed of $n_x n_y$ unit cells. It is therefore asymptotically less than the cost of the classical diffusion. One reason that explains why ρ_3 is much larger than ρ_1 is inherent to MATLAB: The calculation of the matrix of the interface conditions is the only nonvectorized part and is therefore less optimal than the rest of the code. It is therefore expected that an implementation in Fortran and C would increase the ratios ρ_1 and ρ_2. Also, the number of quadrature points N_G in our implementation is the same for calculating all the terms of the matrix. The interactions of far apart nodes could be calculated with a lesser accuracy without modifying the overall accuracy of the calculation and thus improve the cost of the algorithm.

6. PARTICLE TRANSPORT IN VOIDS

This section numerically analyzes the diffusion approximations introduced in the preceding sections for different shapes of the embedded voids.

The domain $\mathcal{D} = (0, 1)^2$ and we assume that the clear inclusion is a rectangle $\mathcal{D}^C = (a, b) \times (c, d) \subset \mathcal{D}$. We define $L_x = (b - a)$ and $L_y = (d - c)$. In all the numerical simulations, the boundary conditions and volume sources vanish everywhere except on the lower side, where the incoming distribution of particles is given by (6). The absorption coefficient is $\sigma_a = \varepsilon$ and the scattering coefficient $\sigma_s = 1/\varepsilon$, where the mean free path ε varies with the simulation. The number of angular directions is $N_a = 128$ and the number of spatial cells $N_x = N_y = 200$. The other parameters of the transport and diffusion solvers are chosen such that the accuracy obtained for each solution is less than 10^{-4}.

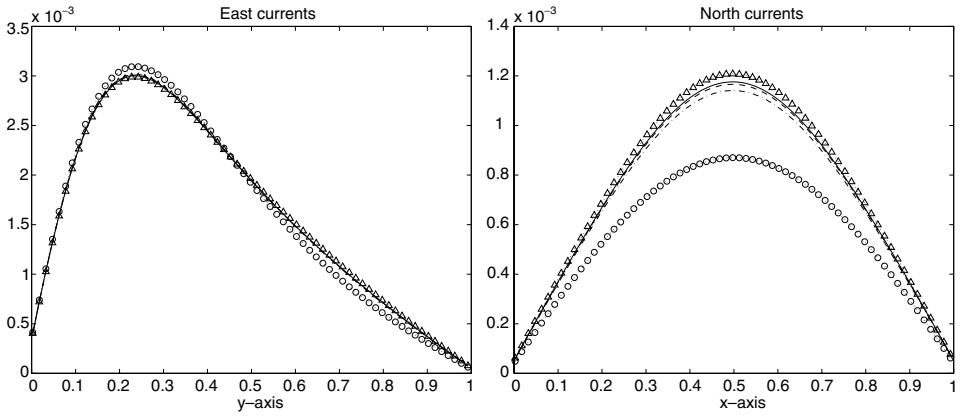

FIG. 3. Currents on the left edge (left figure) and upper edge (right figure) of $\mathcal{D}$ for Test 1. Represented are the transport current $\boldsymbol{J}(\boldsymbol{x}) \cdot \nu(\boldsymbol{x})$ (solid line) and the diffusion currents $D\nu \cdot \boldsymbol{\nabla} u^i(\boldsymbol{x})$ calculated from u^1 (dashed line), u^2 (dot–dashed line), u^3 (dotted line with triangles), and u^4 (dotted line with circles).

6.1. Test 1

In this section we consider a void of the form $\mathcal{D}^C = (0.4, 0.6)^2$. We assume that the mean free path $\varepsilon = 1/50$. We define the control volume $\mathcal{D}_1 = (0.1, 0.9) \times (0.7, 0.9)$ located between the inclusion $\mathcal{D}^C$ and the upper edge of $\mathcal{D}$. Since the inclusion $\mathcal{D}^C$ stands between the incoming source g and the control volume, $\mathcal{D}_1$ is the domain where the diffusion approximations are expected to be the least accurate.

The currents on the upper and left edges are shown in Fig. 3. A horizontal cross section at $y = 0.6$ and a vertical cross section at $x = 0.5$ of the different solutions are given in Fig. 4. The numerical simulation is consistent with theory. Because the volume of the void is significant, replacing it with a diffusive body will change the solution substantially. This is confirmed by the poor quality of the solution u^4. Since the mean free path ε is small compared to the size of the inclusion, the analysis in Section 4.1 applies and the classical diffusion approximation is close to the solution of (9). Therefore, u^3 should be a decent

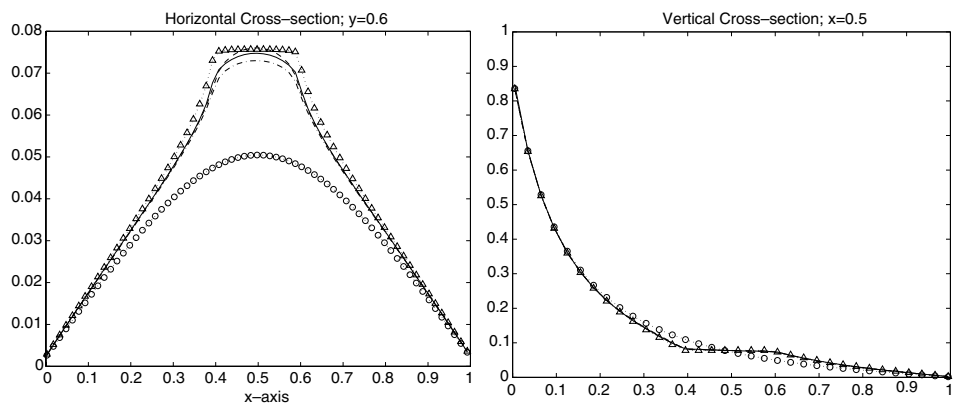

FIG. 4. Horizontal cross section at $y = 0.6$ (left figure) and a vertical cross section at $x = 0.5$ (right figure) of Test 1. Represented are the direction average of the transport solution $U(\boldsymbol{x})$ (solid line) and the diffusion solutions $u^1(\boldsymbol{x})$ (dashed line), $u^2(\boldsymbol{x})$ (dot–dashed line), $u^3(\boldsymbol{x})$ (dotted line with triangles), and $u^4(\boldsymbol{x})$ (dotted line with circles).

TABLE II

L^2-Norm of the Relative Errors e^i_{vol} and e^i_{cur} with $\varepsilon = 1/50$, Test 1

Error	u^1	u^2	u^3	u^4
$\lvert\mathcal{D}_1\rvert^{-1}\lVert e^i_{\text{vol}}\rVert_{L^2(\mathcal{D}_1)}$	7.3×10^{-3}	2.5×10^{-2}	2.8×10^{-2}	0.23
$\lVert e^i_{\text{no}}\rVert_{L^2(0,1)}$	6.9×10^{-3}	2.4×10^{-2}	2.8×10^{-2}	0.22
$\lVert e^i_{\text{ea}}\rVert_{L^2(0,1)}$	3.0×10^{-3}	8.8×10^{-3}	1.6×10^{-2}	9.2×10^{-2}

approximation of the transport equation. Notice the characteristic plateaulike pattern of u^3 that appears in Fig. 4 because u^3 is constant on $\mathcal{D}^C$. Both u^1 and u^2, which have more degrees of freedom than u^3 and incorporate more physics, are also more accurate even though there are theoretically also approximations of order ε of the exact transport solution. This is confirmed by the quantitative volume and current errors given in Table II.

6.2. Test 2

We now consider the case of a mean free path $\varepsilon = 1/100$. The other parameters are the same as for Test 1. The currents on the upper and left edges are shown in Fig. 5. A horizontal cross section at $y = 0.6$ and a vertical cross section at $x = 0.5$ of the different solutions are given in Fig. 6. The volume error and current error on the upper edge are given in Table III.

As expected, the solution u^4 is as inaccurate as for the previous example. All other solutions are more accurate than for Test 1. Since the mean free path has been divided by a factor 2 and the solutions u^1, u^2, and u^3 are all approximations of order ε, we expect the errors to decrease by a factor 2 from Test 1 to Test 2. This is roughly confirmed by the results in Table III. Notice that the constraint $u = \text{Cst}$ inside the inclusion is better satisfied by the transport solution for $\varepsilon = 1/100$ than for $\varepsilon = 1/50$, as can be seen in Fig. 6.

6.3. Test 3

We now present a sequence of numerical simulations where classical diffusion fails to accurately predict the particle density in the whole domain.

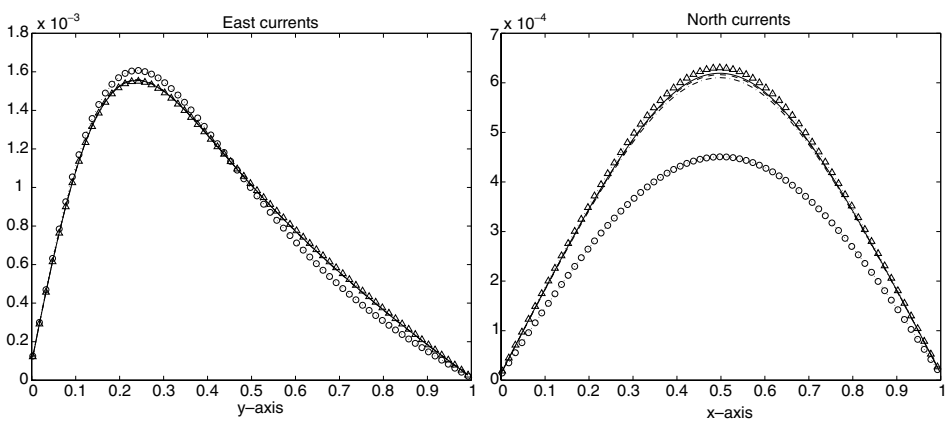

FIG. 5. Same as Fig. 3, for Test 2.

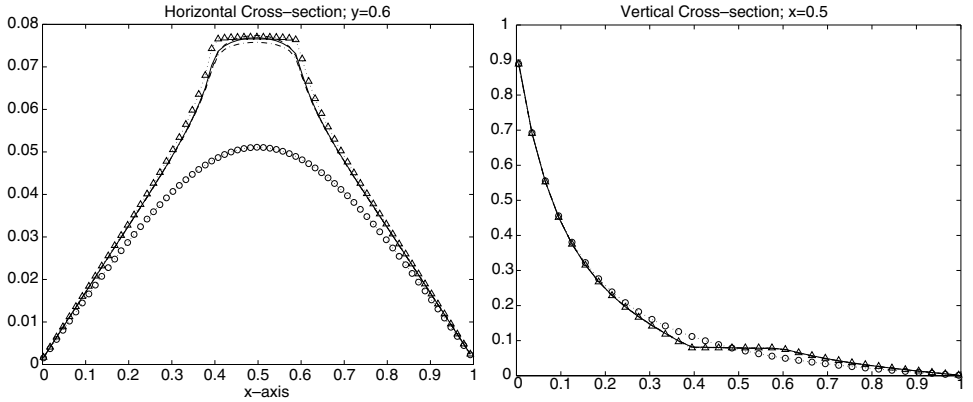

FIG. 6. Same as Fig. 4, for Test 2.

In this third test, the nonscattering inclusion is $\mathcal{D}^C = (0.5, 0.6) \times (0.3, 0.7)$. The value of ε is $1/50$ and the control volume $\mathcal{D}_1 = (0.1, 0.4) \times (0.7, 0.9)$. Notice that $L_x = 5\varepsilon$ and $L_y = 20\varepsilon$. Whereas L_y can be considered as large compared with ε, this is not the case for L_x. Therefore the classical diffusion approximation is expected not to perform too well. This is confirmed by the currents on the upper and left edges of the solution u^3 shown in Fig. 7.

The other solutions, u^1 and u^2, which are predicted by theory to be good approximations of the transport equation both for nonthin and thin extended clear objects, are seen to accurately describe the density inside and outside the transparent inclusion. The horizontal cross section going through the inclusion at $y = 0.6$ and the vertical cross section at $x = 0.2$ of the different solutions are given in Fig. 8. Notice again the flat part of the transport solution and the diffusion solutions u^1 for $i = 1, 2, 3$ inside the inclusion $(0.5 < x < 0.6)$.

The volume error in $\mathcal{D}_1$ and current error on the upper and left edges are given in Table IV. The solutions u^1 and u^2 display a similar accuracy, u^1 being slightly more accurate overall. Whereas u^4 is completely erroneous, the error between the transport solution and u^3 is now about 20%. The classical diffusion approximation overestimates the wave guide property within the clear inclusion (the outgoing flux on the upper edge is too high). A more accurate description of the particle propagation through the inclusion is necessary.

6.4. Test 4

Consider the same inclusion $\mathcal{D}^C = (0.5, 0.6) \times (0.3, 0.7)$ with now $\varepsilon = 1/100$. The currents on the upper and left edges are shown in Fig. 9, the horizontal cross section at $y = 0.6$

TABLE III

L^2-Norm of the Relative Errors e^i_{vol} and e^i_{cur} with $\varepsilon = 1/100$, Test 2

Error	u^1	u^2	u^3	u^4
$\lvert\mathcal{D}_1\rvert^{-1}\lVert e^i_{\text{vol}}\rVert_{L^2(\mathcal{D}_1)}$	4.2×10^{-3}	1.2×10^{-2}	1.8×10^{-2}	0.24
$\lVert e^i_{\text{no}}\rVert_{L^2(0,1)}$	3.9×10^{-3}	1.1×10^{-2}	1.8×10^{-2}	0.23
$\lVert e^i_{\text{ea}}\rVert_{L^2(0,1)}$	1.9×10^{-3}	4.3×10^{-3}	1.0×10^{-2}	0.10

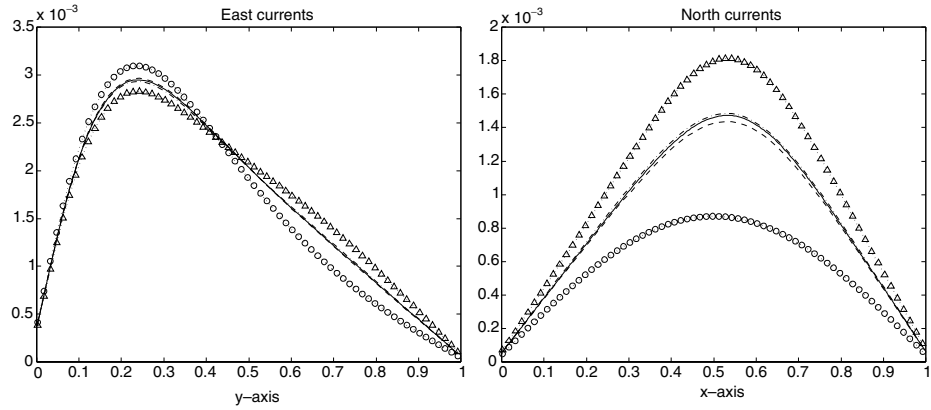

FIG. 7. Same as Fig. 3, for Test 3.

and vertical cross section at $x = 0.2$ in Fig. 10, and the volume error and current error on the upper and left edges in Table V.

We now have $L_x = 10\varepsilon$ and $L_y = 40\varepsilon$. Therefore, L_x becomes relatively large compared with ε, and the theory in Section 4.1 shows that u^3 should become a more accurate approximation. This can be seen by comparing the left hand sides of Figs. 8 and 10. Notice also that the error of u^3 on $\mathcal{D}_1$ reduces from 17 to 11%, which is on the order of ε/L_x, as expected from theory.

The solutions u^1 and u^2, which incorporate more physics, provide an accurate description of the transport solution. Notice here that u^1 is about twice as accurate as u^2. This is because the gradient of the density, which is better accounted for by the model $m = 1$, becomes important along the vertical edges of the inclusion.

6.5. Test 5

The subsequent tests of this section are concerned with very extended inclusions. Consider first the inclusion $\mathcal{D}^C = (0.5, 0.6) \times (0.1, 0.9)$. We set here $\varepsilon = 1/50$. The control volume is $\mathcal{D}_1 = (0.1, 0.4) \times (0.7, 0.9)$.

The same features of the diffusion solutions as before are displayed for this test. The currents on the upper and left edges are shown in Fig. 11. A horizontal cross section at

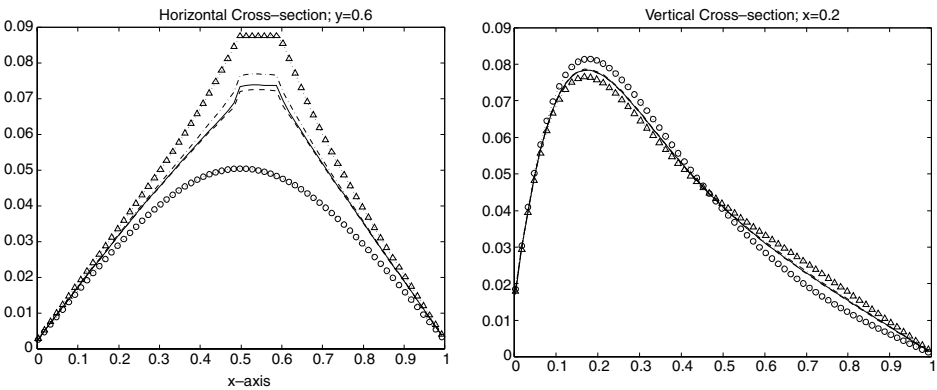

FIG. 8. Same as Fig. 4, for Test 3.

TABLE IV

L^2-Norm of the Relative Errors $e^i_{\rm vol}$ and $e^i_{\rm cur}$ with $\varepsilon = 1/50$, Test 3

Error	u^1	u^2	u^3	u^4
$\lvert\mathcal{D}_1\rvert^{-1}\lVert e^i_{\rm vol}\rVert_{L^2(\mathcal{D}_1)}$	1.1×10^{-2}	1.9×10^{-2}	0.17	0.24
$\lVert e^i_{\rm no}\rVert_{L^2(0,1)}$	1.8×10^{-2}	1.4×10^{-2}	0.20	0.34
$\lVert e^i_{\rm ea}\rVert_{L^2(0,1)}$	7.4×10^{-3}	9.2×10^{-3}	0.11	0.17

TABLE V

L^2-Norm of the Relative Errors $e^i_{\rm vol}$ and $e^i_{\rm cur}$ with $\varepsilon = 1/100$, Test 4

Error	u^1	u^2	u^3	u^4
$\lvert\mathcal{D}_1\rvert^{-1}\lVert e^i_{\rm vol}\rVert_{L^2(\mathcal{D}_1)}$	5.4×10^{-3}	2.2×10^{-2}	0.11	0.29
$\lVert e^i_{\rm no}\rVert_{L^2(0,1)}$	9.0×10^{-3}	2.3×10^{-2}	0.13	0.38
$\lVert e^i_{\rm ea}\rVert_{L^2(0,1)}$	3.7×10^{-3}	1.3×10^{-2}	7.1×10^{-2}	0.20

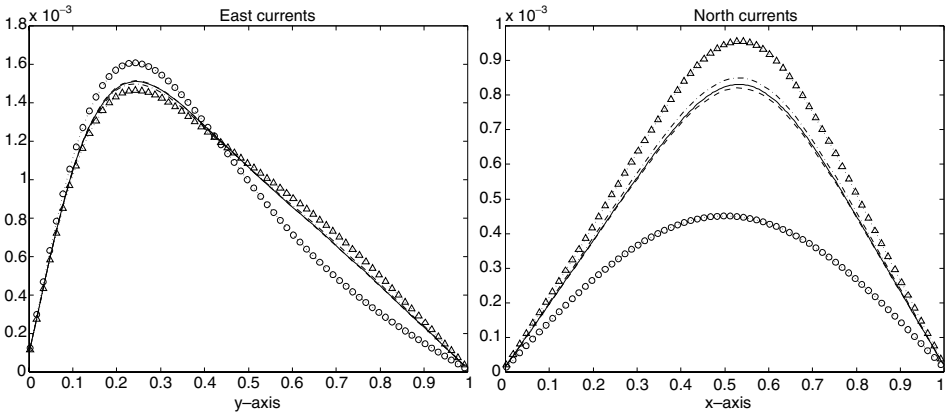

FIG. 9. Same as Fig. 3, for Test 4.

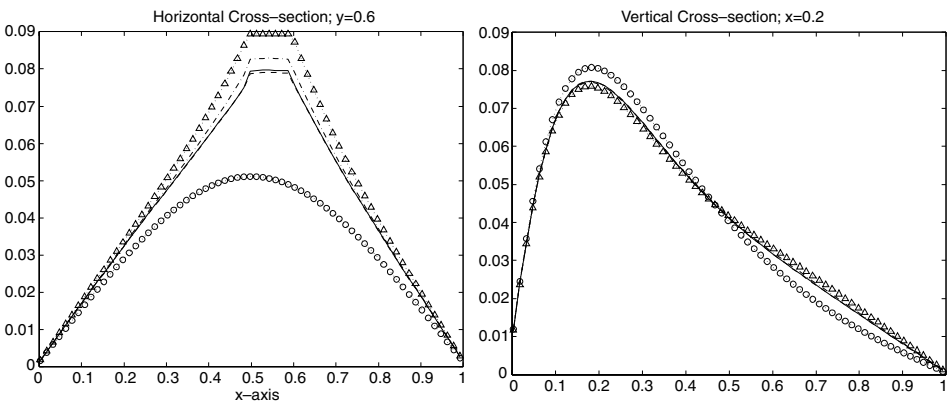

FIG. 10. Same as Fig. 4, for Test 4.

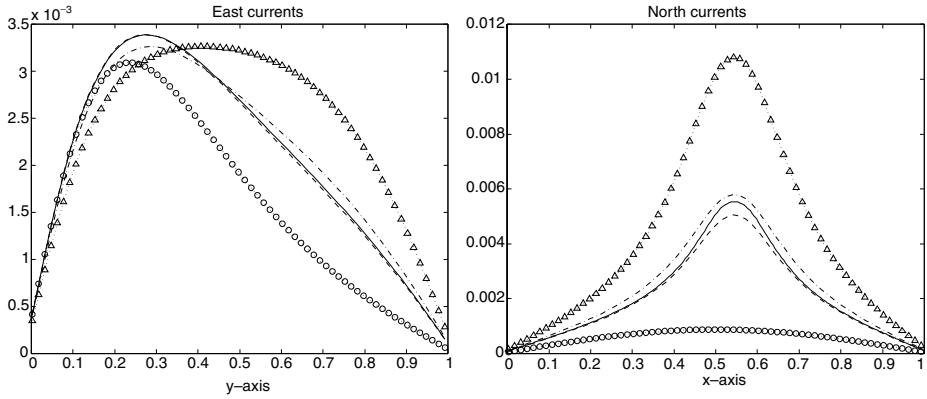

FIG. 11. Same as Fig.3, for Test 5.

$y = 0.6$ and a vertical cross section at $x = 0.2$ of the different solutions are given in Fig. 12. The volume error and current error on the upper and left edges are given in Table VI.

This example is a striking display of the overestimation by classical diffusion of the particle dispersion inside the clear layer. Because the diffusion coefficient is very large within the clear layer, the particle distribution is almost constant on $\partial\mathcal{D}^C$ and the flux of particles crossing the layer much larger than for transport (see the right hand side of Fig. 11). As a result, the error between the transport solution and u^3 reaches 73% on $\mathcal{D}_1$, which renders the classical diffusion solution completely useless.

The two generalized diffusion solutions u^1 and u^2 are good approximations of the transport solution. Notice however that u^1 is now almost 1 order of magnitude better than u^2. This is again due to the presence of large gradients of the density along the vertical edges of the clear inclusion. An asymptotic expansion based on (12) rather than on $u(\boldsymbol{x}, \boldsymbol{\Omega}) \approx U(\boldsymbol{x})$ is then much more desirable.

6.6. Test 6

The parameters of this test are the same as for the previous one, except that now $\varepsilon = 1/100$. The clear layer is 10 mean free paths thick and 80 mean free paths long. The currents on the upper and left edges are shown in Fig. 13. A horizontal cross section at $y = 0.6$ and a vertical cross section at $x = 0.2$ of the different solutions are given in Fig. 14. The volume

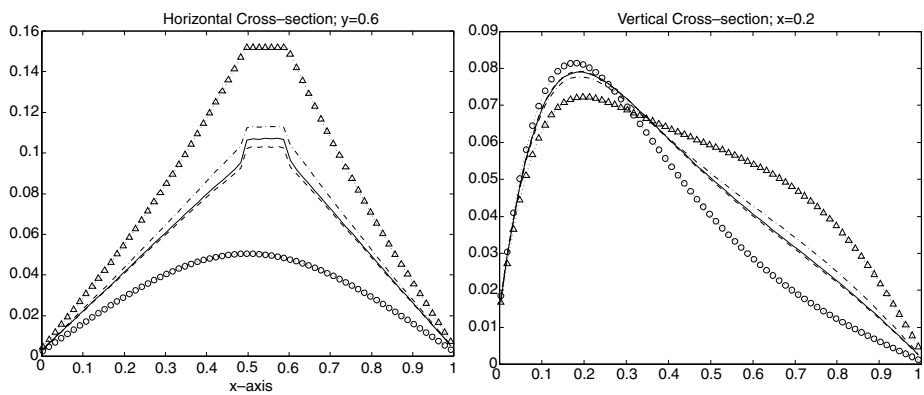

FIG. 12. Same as Fig.4, for Test 5.

TABLE VI

L^2-Norm of the Relative Errors $e^i_{\rm vol}$ and $e^i_{\rm cur}$ with $\varepsilon = 1/50$, Test 5

Error	u^1	u^2	u^3	u^4
$\lvert\mathcal{D}_1\rvert^{-1}\lVert e^i_{\rm vol}\rVert_{L^2(\mathcal{D}_1)}$	2.1×10^{-2}	0.12	0.73	0.50
$\lVert e^i_{\rm no}\rVert_{L^2(0,1)}$	4.1×10^{-2}	1.3×10^{-2}	0.95	0.66
$\lVert e^i_{\rm ea}\rVert_{L^2(0,1)}$	1.4×10^{-2}	7.4×10^{-2}	0.45	0.35

TABLE VII

L^2-Norm of the Relative Errors $e^i_{\rm vol}$ and $e^i_{\rm cur}$ with $\varepsilon = 1/100$, Test 6

Error	u^1	u^2	u^3	u^4
$\lvert\mathcal{D}_1\rvert^{-1}\lVert e^i_{\rm vol}\rVert_{L^2(\mathcal{D}_1)}$	7.4×10^{-3}	0.12	0.47	0.58
$\lVert e^i_{\rm no}\rVert_{L^2(0,1)}$	1.9×10^{-2}	0.14	0.59	0.73
$\lVert e^i_{\rm ea}\rVert_{L^2(0,1)}$	4.5×10^{-3}	7.8×10^{-2}	0.29	0.41

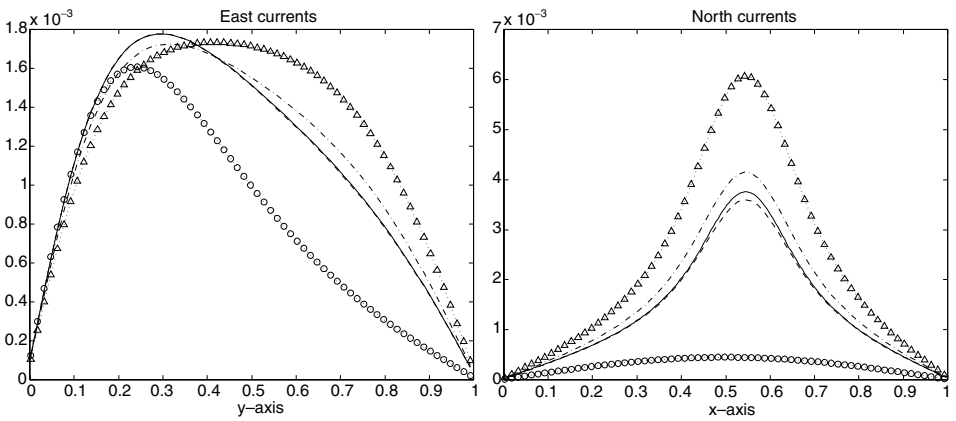

FIG. 13. Same as Fig. 3, for Test 6.

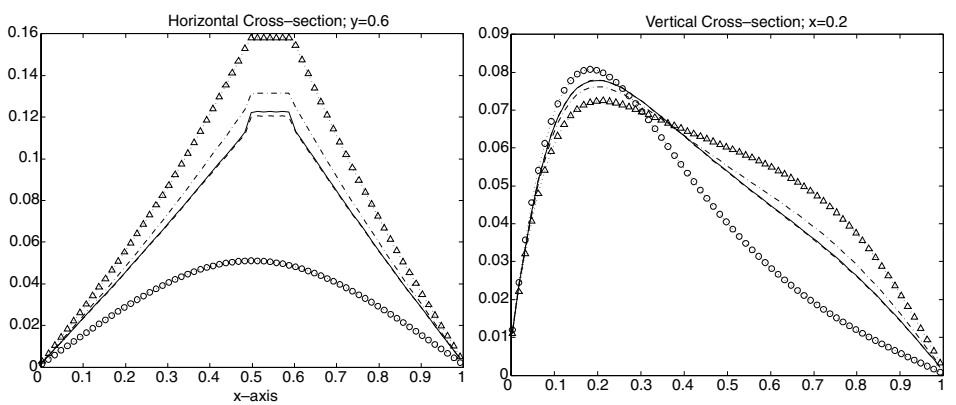

FIG. 14. Same as Fig. 4, for Test 6.

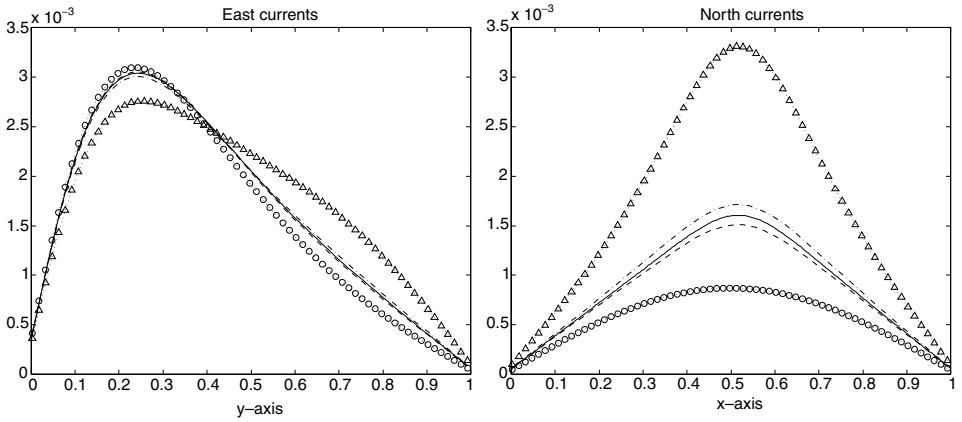

FIG. 15. Same as Fig. 3, for Test 7.

error and current errors on the upper and left edges are given in Table VII. As the mean free path ε goes to 0, u^1 gets closer to the transport solution. However, the solution u^2 for $\varepsilon = 1/100$ does not perform better than for $\varepsilon = 1/50$. The reason, as in the previous case, is that gradients of the flux along the clear layer are quite strong in this test and the model $m = 0$ is not capable of capturing them accurately.

6.7. Test 7

Consider now the thinner inclusion $\mathcal{D}^C = (0.5, 0.55) \times (0.2, 0.8)$. The value of ε is set to $1/50$ and the control volume to $\mathcal{D}_1 = (0.1, 0.4) \times (0.7, 0.9)$.

Again, the currents on the upper and left edges are displayed in Fig. 15, the horizontal cross section at $y = 0.6$ and vertical cross section at $x = 0.2$ of the different solutions are in Fig. 16, and the volume error and current error on the upper edge are in Table VIII.

Most of the comments of Test 5 apply here. The main difference is that because the clear layer is thinner, fewer particles are guided toward the northern edge than in Test 5. As a consequence, the solution u^4, which replaces the inclusion by a diffusive medium, becomes less inaccurate. An error on the order of 30% is still unacceptable in practice. Notice however that it is smaller than the error given by u^3. It is better to *ignore* a thin clear layer than to model it with a classical diffusive model.

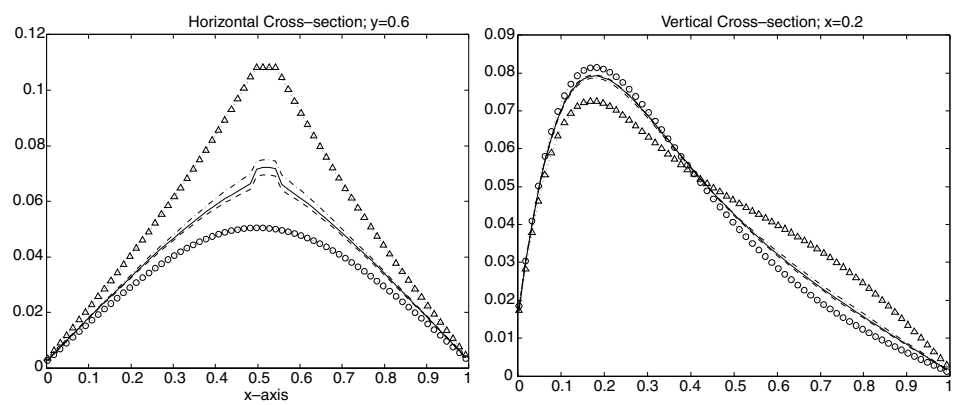

FIG. 16. Same as Fig. 4, for Test 7.

TABLE VIII

L^2-Norm of the Relative Errors $e^i_{\rm vol}$ and $e^i_{\rm cur}$ with $\varepsilon = 1/50$, Test 7

Error	u^1	u^2	u^3	u^4
$\lvert\mathcal{D}_1\rvert^{-1}\lVert e^i_{\rm vol}\rVert_{L^2(\mathcal{D}_1)}$	2.6×10^{-2}	5.8×10^{-2}	0.65	0.26
$\lVert e^i_{\rm no}\rVert_{L^2(0,1)}$	3.9×10^{-2}	6.4×10^{-2}	0.83	0.34
$\lVert e^i_{\rm ea}\rVert_{L^2(0,1)}$	1.5×10^{-2}	2.8×10^{-2}	0.33	0.14

6.8. Test 8

In the last test of this section, the parameters are the same as those of Test 7, except that now $\varepsilon = 1/100$. The currents on the upper and left edges are shown in Fig. 17, the horizontal cross section at $y = 0.6$ and vertical cross section at $x = 0.2$ of the different solutions are given in Fig. 18, and the volume error and current error on the upper edge are given in Table IX. The comments of Test 6 apply here also. Again, the main difference with Test 6 is that u^4 is now more accurate because the clear layer is thinner.

6.9. Conclusions

The diffusion model u^3 gives realistic results only in the case of nonthin inclusions (Tests 1 and 2). For thinner inclusions, the classical diffusion highly overestimates the flow of particles within the clear layer and cannot be used in practice. The solution u^4, where the clear layer is replaced by a diffusive medium and which is given here as a reference, is obviously not a good model either because it overlooks the waveguide effect within the clear layer. It becomes however better than u^3 when the layer is very thin. The models u^1 and u^2, based on generalized interface conditions at the boundary of the layer, correctly account for the dispersion of particles inside the clear layer. Although asymptotically equivalent, the first model, u^1, incorporates more physics and has been shown numerically to be always more accurate than u^2. The reason is that the spatial gradient of the density along the edges of the inclusion is better accounted for by u^1.

Notice however that the solution u^1 is sensibly more expensive to solve and more cumbersome to implement than u^2, as shown in Section 5.2. The difficulty of implementation may

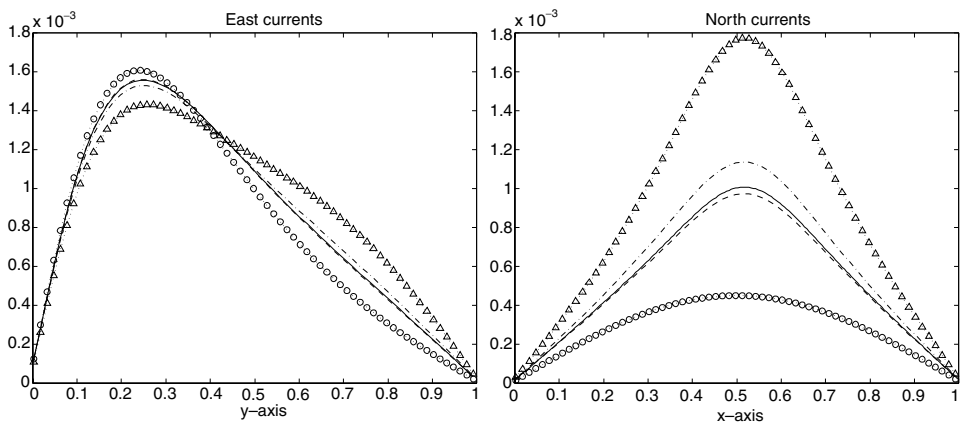

FIG. 17. Same as Fig. 3, for Test 8.

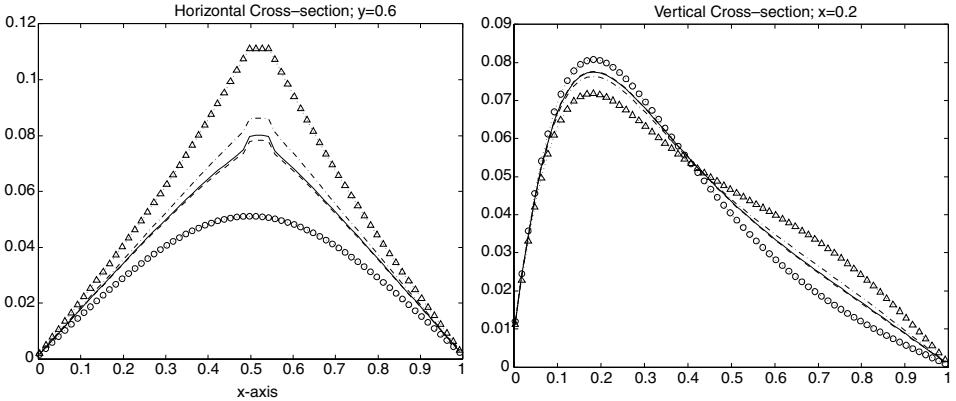

FIG. 18. Same as Fig. 4, for Test 8.

even be amplified for more complex geometries involving curved layers. Whereas solving for u^1 seems necessary for very elongated voids, u^2 offers a good compromise between computation and implementation cost and accuracy for smaller layers.

7. CLEAR LAYERS AND VOIDS IN OPTICAL TOMOGRAPHY

We now consider a setting that models more closely (albeit in two space dimensions) the propagation of NIR photons through scattering regions and voids in an important application of optical tomography. The human head is "modeled" by the domain $\mathcal{D}$ shown in Fig. 2. The clear layer, filled with the cerebrospinal fluid, is $\mathcal{D}^C$. For simplicity, we assume here that it is nonscattering and nonabsorbing, which is a good first approximation. The surrounding human tissues are strongly scattering and weakly absorbing for NIR frequencies ($\mathcal{D}\backslash\mathcal{D}^C$ in Fig. 2). The clear layer is modeled as shown in Fig. 19. Although the Cartesian grid used in the numerical simulations is clearly apparent, realistic clear layers have a nonconstant thickness and the clear layer in Fig. 19 can therefore be seen as a relevant-toy problem.

We consider two numerical simulations. In the first one, the mean free path is $\varepsilon = 1/50$, with scattering coefficient $\sigma_s = 1/\varepsilon$ and absorption coefficient $\sigma_a = \varepsilon$. We introduce two control volumes, $\mathcal{D}_1 = (0.4, 0.6)^2$ and $\mathcal{D}_2 = (0.7, 0.9) \times (0.8, 0.9)$. The currents on the upper and left edges are shown in Fig. 20, the horizontal cross section at $y = 0.6$ and vertical cross section at $x = 0.2$ of the different solutions are in Fig. 21, and the volume errors and current error on the upper and left edges are in Table X.

The clear layer is relatively thin (2.5ε) and its effect should therefore be relatively limited. This is confirmed by the behavior of the solution u^4, obtained by replacing the clear layer

TABLE IX

L^2-Norm of the Relative Errors e^i_{vol} and e^i_{cur} with $\varepsilon = 1/100$, Test 8

Error	u^1	u^2	u^3	u^4
$\lvert\mathcal{D}_1\rvert^{-1}\lVert e^i_{\text{vol}}\rVert_{L^2(\mathcal{D}_1)}$	1.5×10^{-2}	9.4×10^{-2}	0.49	0.34
$\lVert e^i_{\text{no}}\rVert_{L^2(0,1)}$	2.2×10^{-2}	0.11	0.61	0.43
$\lVert e^i_{\text{ea}}\rVert_{L^2(0,1)}$	8.7×10^{-3}	4.9×10^{-2}	0.25	0.19

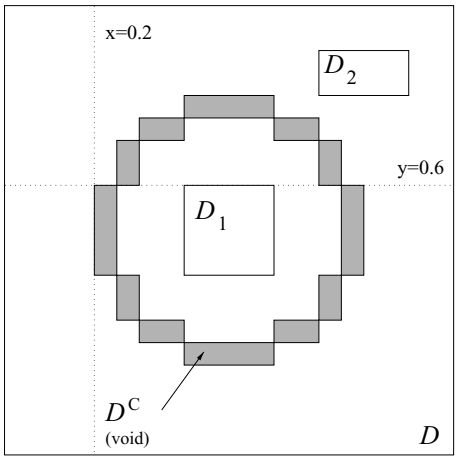

FIG. 19. Geometry of the scattering domain $\mathcal{D} = (0, 1)^2$ with nonscattering clear layer $\mathcal{D}^C$. The thickness of the clear layer is 0.05. The length of the four larger parts is 0.2 and that of the eight remaining ones 0.1.

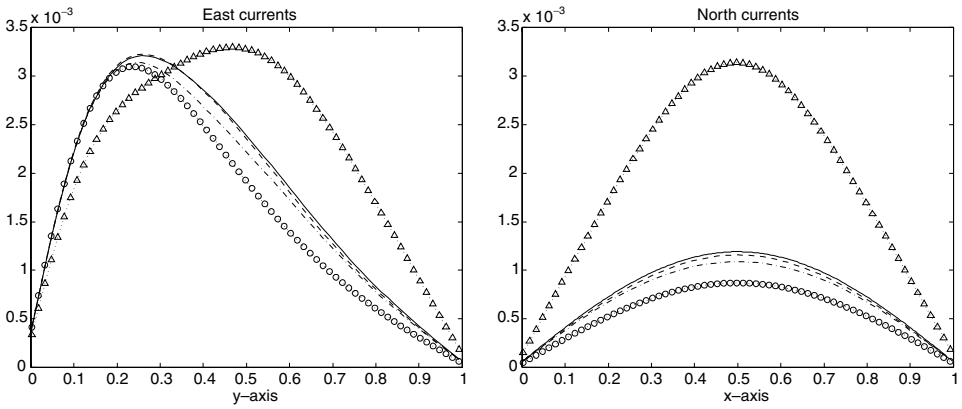

FIG. 20. Same as Fig. 3, for the test of Fig. 19 with $\varepsilon = 1/50$.

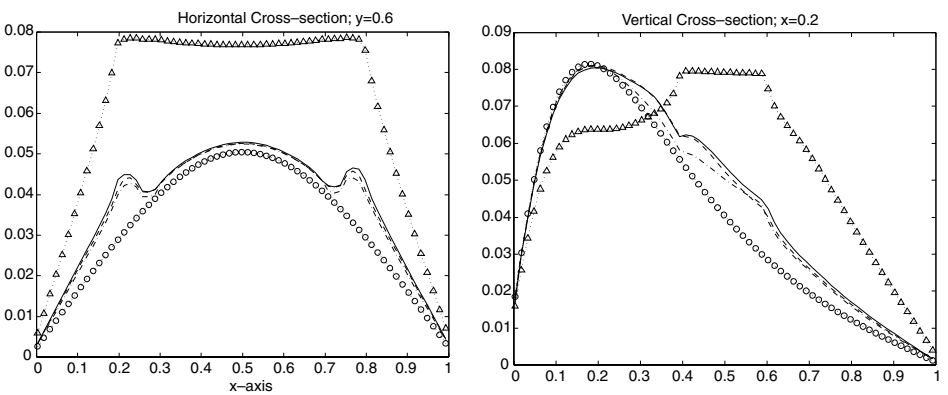

FIG. 21. Same as Fig. 4, for the test of Fig. 19 with $\varepsilon = 1/50$.

TABLE X

L^2-Norm of the Relative Errors e^i_{vol} and e^i_{cur} with $\varepsilon = 1/50$, Test of Fig. 19

Error	u^1	u^2	u^3	u^4
$\lvert\mathcal{D}_1\rvert^{-1}\lVert e^i_{\text{vol}}\rVert_{L^2(\mathcal{D}_1)}$	4.5×10^{-3}	8.4×10^{-3}	0.23	3.3×10^{-2}
$\lvert\mathcal{D}_2\rvert^{-1}\lVert e^i_{\text{vol}}\rVert_{L^2(\mathcal{D}_1)}$	3.8×10^{-2}	7.1×10^{-2}	1.3	0.28
$\lVert e^i_{\text{no}}\rVert_{L^2(0,1)}$	3.4×10^{-2}	7.7×10^{-2}	1.4	0.27
$\lVert e^i_{\text{ea}}\rVert_{L^2(0,1)}$	2.3×10^{-2}	5.5×10^{-2}	0.65	0.20

TABLE XI

L^2-Norm of the Relative Errors e^i_{vol} and e^i_{cur} with $\varepsilon = 1/100$, Test of Fig. 19

Error	u^1	u^2	u^3	u^4
$\lvert\mathcal{D}_1\rvert^{-1}\lVert e^i_{\text{vol}}\rVert_{L^2(\mathcal{D}_1)}$	4.0×10^{-3}	6.1×10^{-3}	0.22	3.9×10^{-2}
$\lvert\mathcal{D}_2\rvert^{-1}\lVert e^i_{\text{vol}}\rVert_{L^2(\mathcal{D}_1)}$	2.9×10^{-2}	2.9×10^{-2}	1.2	0.33
$\lVert e^i_{\text{no}}\rVert_{L^2(0,1)}$	2.9×10^{-2}	3.5×10^{-2}	1.3	0.32
$\lVert e^i_{\text{ea}}\rVert_{L^2(0,1)}$	1.8×10^{-2}	2.6×10^{-2}	0.60	0.23

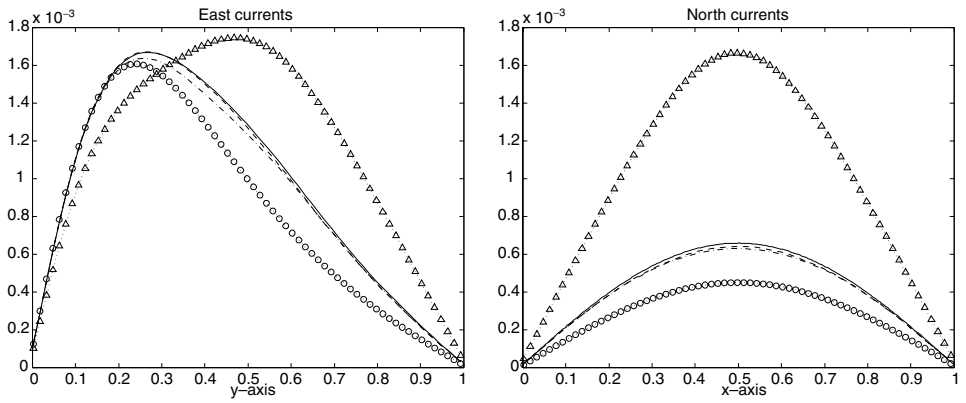

FIG. 22. Same as Fig. 3, for the test of Fig. 19 with $\varepsilon = 1/100$.

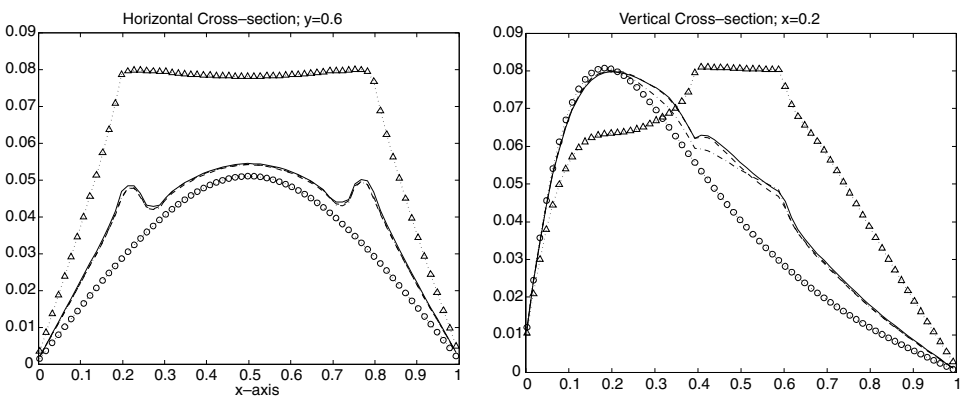

FIG. 23. Same as Fig. 4, for the test of Fig. 19 with $\varepsilon = 1/100$.

by a diffusive medium. The error between the transport solution and u^4 is on the order of 20%. As we have seen in the previous section, the classical diffusion solution u^3 largely overestimates the flow of photons propagating through the clear layer (the current on the northern edge of u^3 is 2.4 bigger than that of the transport solution). Using the classical diffusion solution u^3 is again the worst case scenario.

In spite of the large number of corners and singularities in the clear layer, the solutions u^1 and u^2 provide very decent approximations to the transport solution. Again, u^1 is approximately twice as accurate as u^2, with an error that remains on the order of a few percent, both inside (domain $\mathcal{D}_1$) and on the upper side (domain $\mathcal{D}_2$ and northern current) of the clear layer. The diffusion solution u^1 offers therefore an interesting alternative to computing the transport solution with an error that remains acceptable.

In the second numerical simulation, all coefficients are the same as before, except the mean free path $\varepsilon = 1/100$. The currents on the upper and left edges are shown in Fig. 22, the horizontal cross section at $y = 0.6$ and vertical cross section at $x = 0.2$ of the different solutions are given in Fig. 23, and the volume errors and current error on the upper and left edges are given in Table XI.

The conclusions drawn from the first simulation remain valid for this second simulation. Notice that u^1 and u^2 are closer to the exact solution than in the previous case. This is expected since the mean free path within the diffusive regime is now smaller.

ACKNOWLEDGMENTS

This work was supported in part by NSF Grant DMS-0072008, in part by the ASCI Flash Center at the University of Chicago under DOE Contract B341495, and in part by the MRSEC Program of the National Science Foundation under Award Number DMR-9808595.

REFERENCES

1. M. L. Adams and E. W. Larsen. Fast iterative methods for discrete-ordinates particle transport calculations, *Prog. Nucl. Ener.* **40**(1), 3 (2002).
2. R. E. Alcouffe, Diffusion synthetic acceleration methods for the diamond-differenced discrete-ordinates equations, *Nucl. Sci. Eng.* **64**, 344 (1977).
3. S. R. Arridge, Optical tomography in medical imaging, *Inverse Prob.* **15**, R41 (1999).
4. S. R. Arridge, H. Dehghani, M. Schweiger, and E. Okada, The finite element model for the propagation of light in scattering media: A direct method for domains with nonscattering regions, *Med. Phys.* **27**(1), 252 (2000).
5. S. R. Arridge and J. C. Hebden, Optical imaging in medicine II. Modelling and reconstruction, *Phys. Med. Biol.* **42**, 841 (1997).
6. G. Bal, *Couplage d'Équations et Homogénéisation en Transport Neutronique*, Thèse de Doctorat (de l'Université Paris, 1997).
7. G. Bal, Spatially Varying discrete ordinates methods in XY-geometry, *Math. Models Methods Appl. Sci.* **10**(9), 1277 (2000).
8. G. Bal, Transport through diffusive and non-diffusive regions, embedded objects, and clear layers, *SIAM J. Appl. Math.* **62**(5), 1677 (2002).
9. G. Bal, V. Freilikher, G. Papanicolaou, and L. Ryzhik, Wave transport along surfaces with random impedance, *Phys. Rev. B* **62**(10), 6228 (2000).
10. G. Bal and Y. Maday, Coupling of transport and diffusion models in linear transport theory, *Math. Model. Numer. Anal.* **36**(1), 69 (2002).

11. G. Bal and X. Warin, Discrete ordinates methods in xy-geometry with spatially varying angular discretization, *Nucl. Sci. Eng.* **127**(2), 169 (1997).
12. A. Bensoussan, J.-L. Lions, and G. Papanicolaou, Boundary layers and homogenization of transport processes, *Res. Inst. Math. Sci. Kyoto Univ.* **15**, 53 (1979).
13. C. Börgers, E. W. Larsen, and M. L. Adams, The asymptotic diffusion limit of a linear discontinuous discretization of a 2-dimensional linear transport equation, *J. Comput. Phys.* **98**, 285 (1992).
14. K. M. Case and P. F. Zweifel, *Linear Transport Theory*, Addison-Wesley Series in Nuclear Engineering (Addison–Wesley, Reading, 1967).
15. S. Chandrasekhar, *Radiative Transfer* (Dover, New York, 1960).
16. P. G. Ciarlet, *The Finite Element Method for Elliptic Problems* (North-Holland, Amsterdam, 1978).
17. R. Dautray and J.-L. Lions, *Mathematical Analysis and Numerical Methods for Science and Technology* (Springer-Verlag, Berlin, 1993), Vol. 6.
18. H. Dehghani, D. T. Delphy, and S. R. Arridge, Photon migration in non-scattering tissue and the effects on image reconstruction, *Phys. Med. Biol.* **44**, 2897 (1999).
19. J. J. Duderstadt and W. R. Martin, *Transport Theory* (Wiley-Interscience, New York, 1979).
20. M. Firbank, S. A. Arridge, M. Schweiger, and D. T. Delpy, An investigation of light transport through scattering bodies with non-scattering regions, *Phys. Med. Biol.* **41**, 767 (1996).
21. N. A. Gentile, Implicit Monte Carlo diffusion—An acceleration method for Monte Carlo time-dependent radiative transfer simulations, *J. Comput. Phys.* **172**, 543 (2001).
22. A. H. Hielscher, R. E. Alcouffe, and R. L. Barbour, Comparison of finite-difference transport and diffusion calculations for photon migration in homogeneous and heterogeneous tissues, *Phys. Med. Biol.* **43**, 1285 (1998).
23. A. Ishimaru, *Wave Propagation and Scattering in Random Media* (Academic Press, New York, 1978).
24. E. W. Larsen, The asymptotic diffusion limit of discretized transport problems, *Nucl. Sci. Eng.* **112**(4), 336 (1992).
25. E. W. Larsen and J. B. Keller, Asymptotic solution of neutron transport problems for small mean free paths, *J. Math. Phys.* **15**, 75 (1974).
26. E. W. Larsen and J. E. Morel, Asymptotic solutions of numerical transport problems in optically thick diffusive regimes, ii. *J. Comput. Phys.* **83**, 212 (1989).
27. E. W. Larsen, J. E. Morel, and J. M. McGhee, Asymptotic derivation of the multigroup P_1 and simplified P_N equations with anisotropic scattering, *Nucl. Sci. Eng.* **123**, 328 (1996).
28. E. W. Larsen, J. E. Morel, and W. F. Miller, Jr, Asymptotic solutions of numerical transport problems in optically thick, diffusive regimes, *J. Comput. Phys.* **69**, 283 (1987).
29. E. E. Lewis and W. F. Miller, Jr, *Computational Methods of Neutron Transport* (Wiley, New York, 1984).
30. J. M. Luck and Th. M. Nieuwenhuizen, Light scattering from mesoscopic objects in diffusive media, *Eur. Phys. J. B* **7**(3), 483 (1999).
31. W. H. Press, *et al.*, *Numerical Recipes in C: The Art of Scientific Computing* (Cambridge Univ. Press, Cambridge, MA, 1988).
32. L. Ryzhik, G. Papanicolaou, and J. B. Keller, Transport equations for elastic and other waves in random media, *Wave Motion* **24**, 327 (1996).
33. H. Sato and M. C. Fehler, *Seismic Wave Propagation and Scattering in the Heterogeneous Earth*, AIP Series in Modern Acoustics and Signal Processing (AIP Press, New York, 1998).
34. M. Tidriri, Asymptotic analysis of a coupled system of kinetic equations, *C.R. Acad. Sci. Paris* **328**, 637 (1999).
35. T. A. Wareing, J. M. McGhee, J. E. Morel, and S. D. Pautz, Discontinuous finite element *SN* methods on three-dimensional unstructured grids, *Nucl. Sci. Eng.* **138**(3), 256 (2001).